

# On the use of tracer particles in simulations of binary neutron stars

Luke Bovard<sup>1</sup> and Luciano Rezzolla<sup>1,2</sup>

<sup>1</sup>Institute for Theoretical Physics, Max-von-Laue-Str. 1, 60438 Frankfurt, Germany

<sup>2</sup>Frankfurt Institute for Advanced Studies, Ruth-Moufang-Str. 1, 60438 Frankfurt, Germany

**Abstract.** In grid-based codes that provide the combined solution of the Einstein equations and of relativistic hydrodynamics, the history of the fluid is not simple to track, especially when compared with particle-based codes. The use of tracers, namely massless particles that are advected with the flow, represents a simple and effective way to solve this problem. Yet, the use of tracers in numerical relativity is far from being settled and several issues, such as the impact of different placements in time and space of the tracers, or the relation between the placement and the description of the underlying fluid, have not yet been addressed. In this paper we present the first detailed discussion of the use tracers in numerical-relativity simulations focussing on both unbound material – such as the one needed as input for nuclear-reaction networks calculating r-process nucleosynthesis in mergers of neutron stars – and on bound material – such as the one in the core of the object produced from the merger of two neutron stars. In particular, when interested in unbound matter, we have evaluated different placement schemes that could be used to initially distribute the tracers and how well their predictions match those obtained when using information from the actual fluid flow. Countering our naive expectations, we found that the most effective method does not rely on the rest-mass density distribution nor on the fluid that is unbound, but simply distributes tracers uniformly in rest-mass density. This prescription leads to the closest matching with the information obtained from the hydrodynamical solution. When considering bound matter, we demonstrate that tracers can provide insight into the fine details of the fluid motion as they can be used to track the evolution of fluid elements or to calculate the variation of quantities that are conserved along streamlines of adiabatic flows.

PACS numbers: 04.25.Dm, 04.40.Dg, 95.30.Sf, 95.30.Lz, 97.60.Jd

## 1. Introduction

The recent detection of gravitational waves from binary black hole mergers [1] by LIGO has heralded the era of gravitational-wave astronomy. Detectors such as Virgo, KAGRA, and the Einstein Telescope (ET) [2–4] are expected to detect further events that will allow for a completely new way of observing the universe. An equally exciting possibility is the detection of an electromagnetic counterpart simultaneous with a gravitational wave detection which could help explain the long-standing puzzle of short-gamma ray bursts [5–9]. Although only black hole mergers have so far been detected, binary neutron star (BNS) mergers are expected to be observed in the coming years. As such, significant progress has been made over the last decade to accurately simulate their merger (see, e.g., [10] for a recent review).

A recent area that has received significant interest is the possibility that BNS mergers are the most likely progenitors of the heavy elements in the universe [11–18]. During the merger process, the binary mergers ejects an amount of material that is on the order of  $10^{-2} - 10^{-4} M_{\odot}$  [18–21] and this material exists in an environment that is very conducive towards rapid process neutron capture, r-process, nucleosynthesis [12, 22–25]. Due to a neutron rich environment required for the reactions to occur, the potential astrophysical sites that could produce the r-process elements are limited. For many years, it was thought that core collapse supernova (CCSN) were the source of the heavy elements in our universe [26, 27]. However, recent simulations of CCSN have shown that although CCSN eject sufficient amounts of material, it does not appear to be neutron-rich enough to agree with observations of the abundances observed in the solar system [28]. Furthermore, experimental observations of metallicity in dwarf galaxies disfavors CCSN and instead point towards BNS mergers as being the primary source of r-process [29]. Likewise, recent numerical simulations of BNS mergers with improved neutrino microphysics support the BNS merger scenario as the ejecta from the mergers is very neutron rich [10]. Furthermore, as this ejected material expands, it undergoes radioactive decay and could potentially create an electromagnetic counterpart, the so-called “kilonova” [12, 30, 31]. Hence, there is an increasing interest in studying the composition, evolution and outflow from a BNS merger and the different types of mechanisms that can cause the fluid to undergo nucleosynthesis. There are four types of outflow from a merger that have been considered: dynamical ejecta [20, 25, 32–34], neutrino-driven winds [17, 27, 35–42], magnetically driven winds [43–47], and viscous evolution of the accretion disc [48, 49]. All these ejection channels have different ejection properties which could potentially produce different nucleosynthetic signatures and different light curves emitted from a kilonova, [17, 18, 30, 31, 36–38, 40, 41, 50–52].

In order to study the nucleosynthesis produced from these different categories of ejecta, the thermodynamic history e.g., the temperature, entropy, and electron fraction, of a fluid element is required. These time series are then used as the input for nuclear-reaction networks to determine the abundances of the different elements [27]. However, the timescales required for the nuclear reactions to occur, on the order of seconds to days, is far beyond the current capabilities of numerical-relativity codes, which can run at most a few tens of milliseconds after the merger. In the ideal case, a nuclear-reaction network would be solved simultaneously with the fluid evolution in the simulation, however currently this is numerically infeasible and all nuclear reactions must be treated in a post-processing step. Furthermore, the different ejecta mechanisms have different timescales over which they dominate, ranging from  $\sim 10$  ms for the dynamical ejecta, to  $\sim 1$  s for the viscous ejecta in the disk. This difference in timescales requires different numerical models and assumptions to be made and to overcome these technical issues and various approaches have been used by numerous groups.

One approach is to use Newtonian codes, eschewing general relativity completely [27,

[53]. An advantage of Newtonian codes is that they are computationally and mathematically much simpler and can be run for longer times. Hence, they have been used to study the long-term evolution of the fluid as it outflows, such as that required by the neutrino driven winds – which has timescales of  $\sim 100$  ms [27] – and the viscous forces of the accretion disk [53]. These codes also study the nucleosynthesis produced from the ejecta and the fluid history is recorded by tracer particles (hereafter simply “tracers”). Another approach is to use smoothed particle hydrodynamics (SPH) [16, 27, 51, 52, 54] instead of grid-based codes. One major advantage here is that it allows for exact evolution of the fluid’s thermodynamic properties because the fluid itself is made of interacting particles. While this approach is beneficial for the nucleosynthesis analysis, normally it does not provide solutions in full general relativity. Furthermore this approach cannot be evolved for the long term as the Newtonian codes can. Finally, for grid-based codes which fully solve the Einstein equations, there are two approaches that have been used to follow the thermodynamic history of the ejecta. The first is that of tracers which passively follow the fluid as it evolves recording the properties of the fluid as it evolves [37], providing a history of the fluid lines. The second is to use a spherical surface that the fluid passes through and use that as the initial conditions for the ejecta; assuming the fluid to be undergoing adiabatic expansion, it is then possible to extrapolate the dynamics to long timescales [18]. While both methods can successfully reproduce the r-process, [18, 37, 55], there is a benefit in using the former over the latter. The second method, in fact, is simpler to implement but it does not allow for the history of the fluid element to be recorded. With the thermodynamical history of the fluid element, the tracers are able to be input into radiative-transfer codes that allow for the calculation of kilonova light curves [52]. Thus, it is important that the tracers accurately represent the underlying fluid.

Besides the study of the ejected matter, another area of research in which the use of tracers is particularly beneficial is the evolution of the binary merger product (BMP), that is, of the metastable object that forms after a binary neutron merger. Significant work recently has gone into understanding the nature of the stability of this BMP [10] and tracers provide a novel way of interpreting the resulting behaviour of the BMP that is otherwise inaccessible to only studying the fluid evolution [56, 57].

Although simple in principle, the use of tracers in numerical relativity is far from settled. As observational quantities can be computed from tracer data, it is critical to ensure that the tracers used accurately represent the underlying fluid. As such, many issues such as the effects of placements of the tracers and of assigning tracers mass have not been adequately discussed or settled. Furthermore, tracers are an inherently particle-based idea while the most advanced GR simulations use a grid-based code. Thus relating how tracers properly relate to the underlying fluid requires special care which we discuss in detail. In this paper we present the first detailed discussion of the use tracers in numerical-relativity simulations. We focus on two areas: *unbound material* in the form of dynamical ejecta, and *bound material* in the core of a BMP formed from the merger of two neutron stars. More specifically, when considering unbound matter, we have evaluated four different placement schemes that could be used to initially distribute the tracers and how well their predictions match those obtained when using information from the actual fluid flow. Contradicting our naive expectations that the best placements are those that are correlated with the rest-mass density distribution or that follow the fluid that is marked unbound, we have found that the most effective method is to *uniformly* sample across the rest-mass density distribution as this leads to the closest matching with the hydrodynamical information on the unbound material flowing across the computational domain. On the other hand, when considering bound matter, we have shown that tracers can provide insight into the stability of the BMP as they can be used to track the evolution of fluid elements or to calculate the evolution of quantities conserved along

streamlines that would otherwise be inaccessible in a grid-based code [56, 58].

The paper is organised as follows: in Sec. 2 we review the mathematical and numerical setup employed to solve the equations of relativistic hydrodynamics but also those describing the motion of the tracers and their analysis. Section 3 is instead dedicated to the study of the dynamics of unbound material and to the discussion of the various placement schemes that we have considered. The results in this section should be contrasted with those presented in Sec. 4 for bound material, where we analyse tracers in the core of an HMNS produced by a BNS merger. Finally, in Sec. 5 we summarise our results and discuss their applicability to future work. Unless otherwise specified, we use a system of units such that  $c = G = M_\odot = 1$ , where  $c$  is the speed of light in vacuum,  $G$  is the gravitational constant, and  $M_\odot$  is the mass of the Sun. We use Einstein's convention of summation over repeated indices. Latin indices run over 1, 2, 3, while Greek indices run over 0, 1, 2, 3. The spacetime metric signature we adopt is  $(-, +, +, +)$ .

## 2. Mathematical and numerical setup

### 2.1. Relativistic hydrodynamics and neutrino transport

Einstein's theory of general relativity can be written as

$$R_{\mu\nu} - \frac{1}{2}Rg_{\mu\nu} = 8\pi T_{\mu\nu}. \quad (1)$$

In order to solve the above equations, we use the 3+1 decomposition

$$ds^2 = -(\alpha^2 - \beta_i\beta^i)dt^2 + 2\beta_idx^i dt + \gamma_{ij}dx^i dx^j, \quad (2)$$

where  $\alpha$  is the lapse,  $\beta_i$  is the shift vector, and  $\gamma_{ij}$  is the 3-metric [59]. We then decompose the spacetime into a conformal-traceless 3+1 formulation known as the BSSNOK formulation of the Einstein equations [60–62]. This decomposition deals with the spacetime, but to simulate BNS mergers, we require a description for the underlying matter. To do so, we model the neutron stars as perfect fluids, where the energy-momentum tensor is given by

$$T_{\mu\nu} := (e + p) u_\mu u_\nu + p g_{\mu\nu}, \quad (3)$$

where  $u^\mu := dx^\mu/d\tau$  is the four velocity of the fluid with position  $x^\mu$  and proper time  $\tau$ ,  $e$  is the energy density, and  $p$  is the pressure. In order to include neutrinos, we must take into account weak interactions, which can change the composition of the material. Without weak interactions, the baryon number is conserved, however when they are included, a source term must be added to the conservation equation, which can be written as

$$\nabla_\alpha(n_e u^\alpha) = R, \quad (4)$$

where  $n_e$  is the electron-number density and where  $R$  is the net lepton number emission/absorption rate per unit volume in the fluid rest-frame. Likewise, the conservation of energy and momentum now becomes, with the introduction of sources

$$\nabla_\beta T^{\alpha\beta} = Qu^\alpha, \quad (5)$$

and  $Q$  is the net neutrino cooling/heating rate per unit volume in the fluid rest-frame [18]. A detailed discussion on the computations of  $Q$  and  $R$  within the code employed here is contained in Refs. [18, 63]. In order to close the system of equations (4) and (5) an equation of state (EOS) of the form  $p = p(\rho, \epsilon, Y_e)$  is required, where  $\rho$  is the rest-mass density,  $\epsilon$  is the specific internal energy, and  $Y_e$  is the electron fraction. The EOSs we use are the LS220 EOS of [64] with a nuclear compressibility parameter  $K = 220$  MeV and the DD2 EOS [65].

These EOSs have been used extensively in numerous simulations, e.g., [10, 18, 56, 63] and provide useful test cases.

To solve the spacetime equations numerically we use the `Mclachlan` code [66] which is part of the `Einstein Toolkit` [67]. The hydrodynamics are solved using the `WhiskyTHC` code [68, 69]. `WhiskyTHC` implements finite-volume and finite-difference with high-resolution shock-capturing methods and has been used extensively to study BNS mergers.

## 2.2. Initial data and grid setup

We have considered two types of initial data for the simulations depending on whether our analysis focuses on unbound or bound material. In both cases, however, the BNSs refer to an irrotational flow and were computed using the multi-domain spectral-method code `LORENE` [70] under the assumption of a conformally flat spacetime metric and employing the EOS at beta-equilibrium. For the study of the *unbound material* we used quasi-circular initial data – at least four orbits – with an initial gravitational mass of  $M = 1.35 M_\odot$  and initial separation of 45 km with the LS220 EOS. For the bound material, on the other hand, we have again chosen quasi-circular initial data with a gravitational mass of  $M = 1.35 M_\odot$  and initial separation of 45 km but with the DD2 EOS. The reason for choosing a different EOS is that DD2 is stiffer than LS220 and collapses to a black hole at a later time allowing sufficiently long timescales to investigate the structure of the core before collapse. Because the fluid that becomes unbound is located far away from the merger site, e.g., at distances  $\gtrsim 300$  km from the centre of the grid, a higher resolution is desirable to better capture the fluid. For this reason, a resolution of  $\Delta h_5 = 0.15 M_\odot \approx 220$  m for the finest refinement level was used for the unbound material evolution and  $\pi$ -symmetry imposed. For the bound material, resolution is not as important for investigating some aspects of the fluid properties, see, e.g., [56], but for completeness  $\Delta h_5 = 0.15 M_\odot \approx 220$  m was also used for the finest refinement level but with no  $\pi$ -symmetry to ensure that the one-arm stability is allowed to develop [71]. Both simulations had five refinement levels, reflection symmetries, and an outer boundary of  $512 M_\odot \approx 760$  km.

## 2.3. Tracer evolution

In order to follow the evolution of the fluid, we place tracers in the fluid which are able to record the properties of the fluid at a given point. These tracers are massless, see Sec 2.4, and are passively advected through the equation [72, 73]

$$\frac{d\vec{x}}{dt} = \vec{v}, \quad (6)$$

where the velocity vector  $\vec{v}$  refers to the three-velocity of the fluid with respect to the coordinates. In the 3+1 formalism this velocity is related to the fluid velocity through

$$\vec{v} := \alpha \vec{v} - \vec{\beta}, \quad (7)$$

with  $\alpha$  the lapse,  $\vec{v}$  the three-velocity of the fluid, and  $\vec{\beta}$  the shift vector. We solve Eq. (6) with a simple forward Euler scheme where the  $\Delta t$  is equal to the time-step of the finest grid. In our simulation, this equation can be solved for a variable number of tracers  $N_t$  and we have chosen to set  $N_t = 10^5$  throughout. Furthermore, since the tracers do not interact and are considered point particles they can, in principle, occupy the same coordinates; in practice, however, this does not happen in the simulations we have performed. As the tracers pass through the grid, the value of various variables is recorded. Since the variables are computed only on the grid

points, and in general the tracers will not be on the grid points, the desired properties are interpolated to the  $(x, y, z)$  position of the tracer. Specifically, the most important quantities for nucleosynthesis are  $(\rho, T, Y_e)$ , which are evolved through the main evolution code.

#### 2.4. Tracer mass flux

As mentioned above, the main goal of studying the unbound material is to use the tracers as input for nuclear-reaction networks. When the tracers are post-processed through a nuclear-reaction network, the resulting distribution of the abundancies must be weighted in some way. To do this, a “mass” must be associated to each tracers. In contrast to SPH codes, where the tracers explicitly represent the underlying fluid and can have a mass, the tracers we employ are *massless* and attention needs to be paid when wanting to assign a “mass” to an individual tracer. In some fully general-relativistic works, e.g., Ref. [73], tracers have been assigned an associated mass; this concept, however, is potentially misleading. First, since tracers play only a passive role without a coupling to the fluid besides that of following the advection equation (6); assigning a mass to the tracers breaks these assumptions. Second, if a tracer is initially associated with a mass based on its surroundings, then at later times this mass cannot represent the same mass it did initially since the underlying properties will have changed. For example, if the initial mass is calculated from the rest-mass density where the tracer is initially at, then at a later time the density will have decreased significantly and no longer represents the same mass as it did before. Finally, in order to calculate a mass from a density, some volume must be specified and tracers represent idealised point particles.

Having made these remarks, and since nucleosynthesis calculations require masses to weight the different abundance curves, a scheme to assign a “mass” with the tracers is necessary. Our proposal for such a scheme avoids all of the above issues by calculating the flux of the tracers through a given 2-sphere of coordinate radius  $R$ , which we take to be  $200 M_\odot \approx 295 \text{ km}$  [18, 55]. We can therefore define the “tracer mass current” at a given iteration  $i$  as

$$\vec{j}_i := \vec{j}(\vec{x}, t_i) = \rho W(\alpha\vec{v} - \vec{\beta}) = \sum_j W_j(\vec{x}, t) \rho_j(\vec{x}, t) \vec{v}_j(\vec{x}, t), \quad (8)$$

where we sum over the tracers that cross through a surface of a given radius during that iteration. Because we evaluate the flux far from the BMP, the geometry is approximately flat, i.e.,  $\alpha \simeq 1, \vec{\beta} \simeq 0$ , so that the final special-relativistic expression (8) provides a good approximation. As the information about the velocity, Lorentz factor, and the rest-mass density are recorded, we have a way to associate a flux with the tracers crossing the surface. Integrating over the surface at a given time allows us to define a “tracer mass flux” as

$$\dot{M}_i(t) = \oint \vec{j}_i \cdot \vec{n} \sqrt{\gamma} dS = \oint \vec{j}_i \cdot \vec{n} dS, \quad (9)$$

where we take the surface element on a sphere to be  $dS = r^2 \sin \theta d\theta d\phi$  and again taking the special relativity expression since we are sufficiently far away from the BMP. Then we are able to obtain a simple differential equation

$$\frac{dM_{\text{tr}}}{dt} = \dot{M}, \quad (10)$$

for the tracer mass flux which can be integrated to obtain a mass associated with the tracers. We stress that this “mass” is only valid as the tracers pass through the surface and does not represent the true mass unbound that would be measured when calculating the flux of the underlying fluid through a sphere. In Sec. 3.4 we will compare the mass flux computed

via the tracers, i.e., Eq. (10), with the corresponding quantity computed using standard hydrodynamical quantities, e.g., the rest-mass current, and demonstrate that this method can reasonably well approximate that of the “exact” answer from the underlying fluid. In contrast, for the bound material, we are only interested in following the streamlines of the fluid, which is the most fluid dynamical role that passively advected tracers play. In this case, the mass of the tracers is irrelevant.

### 3. Tracing unbound material

We start our discussion on the use of tracers by considering the case in which they are employed to describe the dynamics of matter that is gravitationally *unbound*. Obviously, due to the finite computational domain, tracers cannot escape further than the outer boundary of  $512 M_{\odot}$  and thus we must have a criterion that records whether or not the tracers will escape to infinity. To do this, we follow the geodesic criterion, i.e., we consider a tracer to be unbound when the corresponding fluid element has the covariant time component of the four-velocity  $u_t \leq -1$ , which corresponds to considering tracers as moving on geodesics and reaching infinity with zero energy [59]. Other criteria could be used, such as the Bernoulli criterion  $hu_t \leq -1$ , which has been explored, for instance, in Ref. [49]. Here however, we have only made use of the geodesic criterion as it is sufficiently robust, does not require any tuning and generically does lead to rather conservative measurements of the mass losses (a more detailed discussion will be presented in Ref. [55]).

In practice, every tracer records the value of the underlying fluid’s  $u_t$  at that point and it is then determined in a post-processing stage whether or not the tracer should be counted for comparison with the fluid quantities. It is also important to ensure that the tracer satisfies the geodesic criterion at all points, since it is possible for the tracer to become unbound, then undergo shock heating and become rebound. In a post-processing step, every tracer is checked to ensure that once the tracer becomes unbound, it remains unbound. Finally, due to the high velocity of the ejecta, tracers can easily reach the boundary of the grid and, in this case, the tracer properties are set to atmosphere values and dealt with in a post-processing step.

We next discuss an often neglected aspect of the treatment of tracers, namely, their initial placement. Despite this being a very important step, as it can significantly influence the overall results recorded by the tracers, this is the first time that a systematic discussion is made, at least to the best of our knowledge. The material that we present in the following sections is admittedly detailed and the reader who is not particularly interested in the more technical aspects can skip such material and concentrate on the concluding remarks at the end of Sec. 3.4 (see text in italics).

#### 3.1. Initial placement

The final goal here is to accurately capture the essential properties of the underlying fluid in the tracers. In order to properly represent the underlying fluid, we need to ensure that we are sampling the fluid in a sufficiently accurate manner. The important first step is to ensure that when we initially place the tracers, we are sampling the material that is most likely to become unbound. However, different placements of the tracers initially can potentially lead to different representative properties. One potential placement scheme, which was followed in Refs. [39, 73], is to place more tracers where there is higher rest-mass density. This process is done randomly with more tracers being placed at higher densities and fewer at lower densities. Foucart et al. [72] have successfully used tracers to measure fluid properties but no discussion is made on the initial placement procedure. Finally, Wanajo et al. [37]

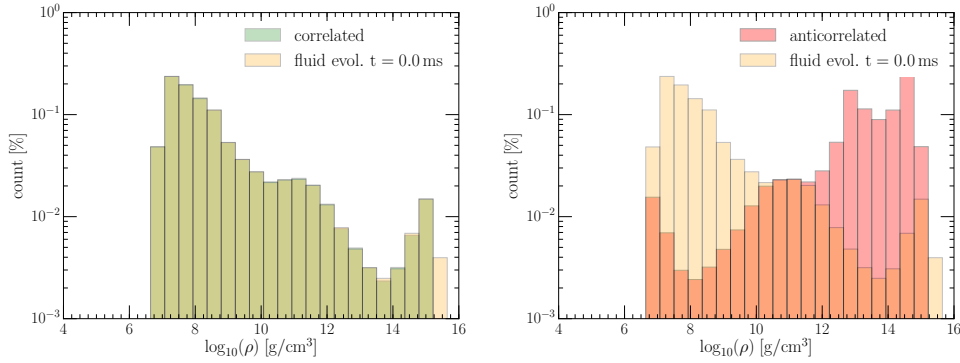


**Figure 1.** Histograms showing the distribution of the underlying rest-mass density of the fluid (light-yellow shade) compared with the initial placement of the tracers for the “correlated” (green) and the “anticorrelated” (red). The histograms are normalised with respect to the total number of cells for the fluid and  $10^5$  for the tracers. The placement is done at merger.

have used tracers in their study of r-process nucleosynthesis, focussing however only on the  $(x, y)$ ,  $(y, z)$ , and  $(x, z)$  planes; also in this case no discussion is made on the impact of the placement of the tracers on their conclusions. Thus how effective tracers are with respect to the underlying fluid and how their results would change if they change the initial placement has been unexplored. In what follows we discuss three different placement schemes and the corresponding dynamics.

Before deciding *where* to place the tracers, we must decide *when* they should be first distributed. Luckily, when studying BNS merger, the most natural selection of placement time is straightforward: at the merger. Prior to the merger, in fact, there is no mass outflow, beyond some small spurious outflow due to initial conditions and the inevitable and tenuous mass loss at the stellar surface. Another timing option is to let the simulation evolve for a few milliseconds after merger, which is when much of the dynamical ejecta is produced, and then place the tracers to best capture this material. Once this optimal time is fixed, we need a way to distribute the tracers. A priori, there is no obvious “best choice” for what the correct initial placement of tracers is. However, since we are also interested in using the tracer flux to get a representative mass, choosing a scheme that is based on an initial rest-mass density distribution does have merit. Furthermore, it is reasonable to expect that low rest-mass density material around the merging stars are going to be good candidates for material that will become unbound. Conversely, we do not expect material at the high densities in the core of the merger product to be ejected in contrast with the schemes of [39, 73]. Material inside the neutron star that is between these two extremes can still be ejected due to the complicated merging process, which can eject material from within the neutron star.

In light of these considerations, at the chosen time during the simulation we fix a Cartesian box surrounding the BMP and place tracers at the grid points within this box, distributed according to a scheme that is weighted with some probability distribution. In practice we have considered four different options that we discuss in detail below.

**3.1.1. Tracers correlated/anticorrelated** Firstly, we consider the most natural probability distribution, namely, placing tracers using a distribution function which is directly correlated to the rest-mass density distribution at merger. In other words, within our fixed box we count the number of cells within a given rest-mass density range, then normalise by the total



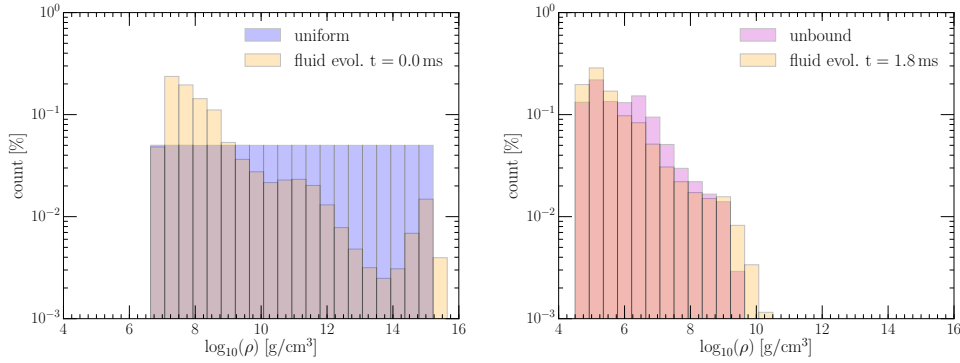


**Figure 2.** *Left:* Histograms showing the distribution of the underlying rest-mass density of the fluid (light-yellow shade) compared with the initial placement of the tracers for the uniform (blue). The histograms are normalised with respect to the total number of cells for the fluid and  $10^5$  for the tracers. The placement is done at merger. *Right:* The same as in the left panel but showing the distribution of the underlying rest-mass density of the fluid (light-yellow shade) compared with the placement of the tracers for the  $u_t$  placement scheme (purple). The histograms are normalised with respect to the total number of cells for the fluid and  $10^5$  for the tracers. The placement is made 1.8 ms after the merger.

number of cells, and finally bin them appropriately making sure that no more than one tracer is assigned to a given cell.

In both panels of Fig. 1, the light-yellow shaded distribution represents the underlying rest-mass density distribution produced by the fluid evolution and calculated directly from the grid data. Note that the fluid rest-mass density ranges from  $\sim 10^{15}$  g/cm<sup>3</sup> in the core out to  $\sim 10^7$  g/cm<sup>3</sup> in the material around BMP, which represents approximately 20% of the rest-mass density cells. Note also that in our simulations the atmosphere is set at  $\sim 6 \times 10^3$  g/cm<sup>3</sup> [68, 69] and the lowest rest-mass density of initial placement is at least three orders of magnitude larger so no tracers are placed at the atmosphere. The left panel of Fig. 1 compares the rest-mass distribution computed from the fluid evolution with the one adopted for the tracers, to which it is “*correlated*” within a rest-mass density range (light-green shade). More specifically, the lower rest-mass density is set to the same as the fluid while the upper rest-mass density is taken to be  $10^{15}$  g/cm<sup>3</sup>. We then select  $10^5$  cells randomly from the underlying fluid bins. The variations between the “*correlated*” distribution and that of the fluid are very small and are negligible, with the only difference occurring just below  $10^{14}$  g/cm<sup>3</sup> where the fewest number of fluid cells with that rest-mass density exist.

This behaviour should be contrasted with the one obtained when the tracer distribution is “*anticorrelated*” with the rest-mass density and that is shown in the right panel of Fig. 1 (light-red shade). In practice, we first randomly selected from the higher densities and then randomly filled in the lower densities, thus resulting in an almost reflected distribution from the underlying distribution. This procedure also saturates some of the higher rest-mass densities, for which a tracer placed at every cell leads to a flattening of the distribution in the high rest-mass density region. At lower densities, on the other hand, we do see an increase in the distribution which is due to the random selection.

**3.1.2. Tracers uniformly distributed** The third placement we consider at the merger is the uniform distribution. In this case, we equally divide the tracers into the 20 bins that the underlying fluid was divided into. This results in a distribution that does not follow the

underlying rest-mass density distribution at all, but instead places an equal number of tracers at all densities. The resulting distribution is shown in the left panel of Fig. 2 (light-blue shade) and when comparing with the underlying fluid (light-yellow shade) we can clearly observe that this placement oversamples the higher densities (i.e.,  $\gtrsim 10^{10}$  g/cm<sup>3</sup>) while it undersamples the lower densities (i.e.,  $\lesssim 10^8$  g/cm<sup>3</sup>).

*3.1.3. Tracers following unbound matter* The last placement we considered is different from the previous three in at least two important aspects. First, a proper choice needs to be made about the time of placement. To this scope, we required that the initial dynamical outflow had not yet passed the  $200 M_{\odot}$  radius, which is where we collect information about the underlying fluid through a spherical surface placed to measure the outgoing flow [18]. This time worked out to be 1.8 ms after the merger; at this time the dynamical ejecta are close to, but have not passed the  $200 M_{\odot}$  radius. Second, instead of placing the tracers based on the rest-mass density, we placed them based on  $u_t$  and only considered cells where  $u_t \leq -1$ , i.e., at that time the cell represented unbound material. Then, we randomly selected  $10^5$  of those cells and placed a tracer at that location. The resulting distribution is shown in the right panel of Fig. 2 (light-purple shade) and it is interesting to note that even though we distributed the tracers based on  $u_t$ , the distribution still has approximately the same structure as that of the evolved fluid<sup>‡</sup>. The main differences are that it overshoots in the rest-mass density between  $10^6 - 10^8$  g/cm<sup>3</sup> and does not place tracers at higher densities of  $10^{10}$  g/cm<sup>3</sup>. This is likely due to the fact that higher rest-mass density material is closer to the BMP and less likely to be unbound. Also note that the underlying fluid distribution densities extend above rest-mass densities of  $10^{10}$  g/cm<sup>3</sup> but do not appear in the right panel of Fig. 2 because the latter maintains the same dynamic range of the other three panels in Figs. 1 and 2.

### 3.2. Three-dimensional dynamics of unbound tracers

In order to perform the nucleosynthesis calculations, the material that is ejected has to have had sufficient time to become unbound and for this reason all of the simulations presented here have been run for at least 10 ms after merger. When using the geodesic criterion, in fact, there is essentially no flux of unbound material or of tracers<sup>§</sup> through a 2-sphere of radius  $200 M_{\odot}$ ; 10 ms are also a sufficient time for the tracers and the fluid to reach the outer boundary of our computational domain. In Fig. 3 we show a visualisation of the tracers for the four different placement schemes discussed above (from top to bottom: “correlated”, “anticorrelated”, “uniform”, and “unbound”) at three different times corresponding roughly to when the unbound material passes through spheres of radii 200, 300,  $500 M_{\odot}$  (i.e.,  $t \sim 2, 3,$  and 7 ms after the merger, respectively). On the  $(x, y)$ ,  $(y, z)$ , and  $(x, z)$  planes are shown the values of the rest-mass density using the colourbar in the left lower corner. A colourbar on the right lower corner is also used to visualise the rest-mass density of the fluid elements hosting the tracers. Note the different colour scales for the fluid and the tracers.

For the case of “correlated” tracers (first row), we can see the presence of a large number of tracers at high latitudes, which correspond to those initial tracers that are at low rest-mass density. This is to be contrasted with the dynamics of “uncorrelated” tracers (second row), which shows the anticorrelated placement which has significantly fewer tracers at higher latitudes and closer to the BMP, simply as a result of having downsampled fluid elements at

<sup>‡</sup> Note that the distribution coming from the fluid evolution is different than that on the left panel of Fig. 2 since it refers to a different time in the simulation.

<sup>§</sup> This is not necessarily the case when using the Bernoulli criterion, which is less restrictive and allows for mass being ejected also at later times [55].

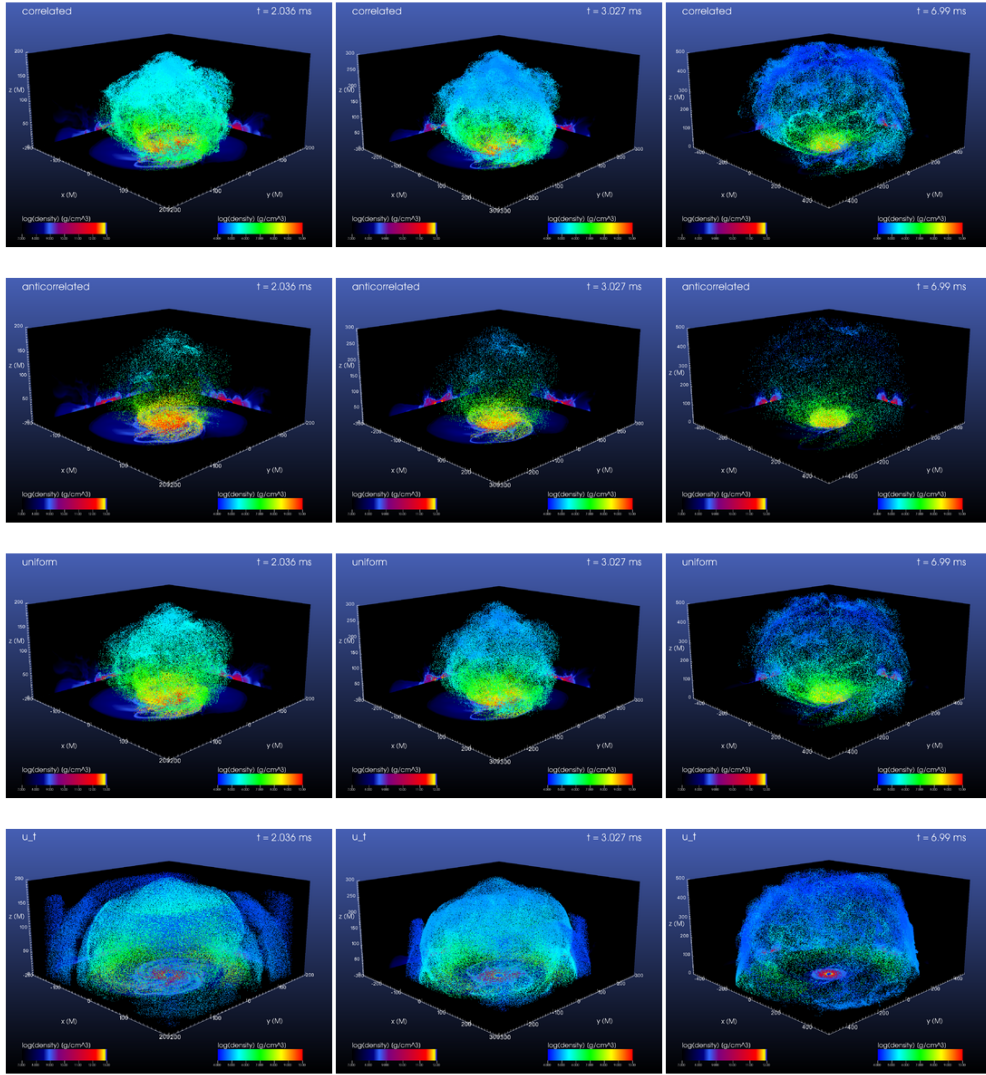


**Figure 3.** Visualisation of the tracers for four different placement schemes (top to bottom) at three different times (left to right). From top to bottom: “correlated”, “anticorrelated”, “uniform”, and “unbound”. From left to right to  $\sim 2, 3, 7$  ms after merger. On the  $(x, y)$ ,  $(y, z)$ , and  $(x, z)$  planes are shown the values of the rest-mass density using the colourbar in the left lower corner. A colourbar on the right lower corner is also used to visualise the rest-mass density of the fluid elements hosting the tracers. Note the different colour scales for the fluid and the tracers.

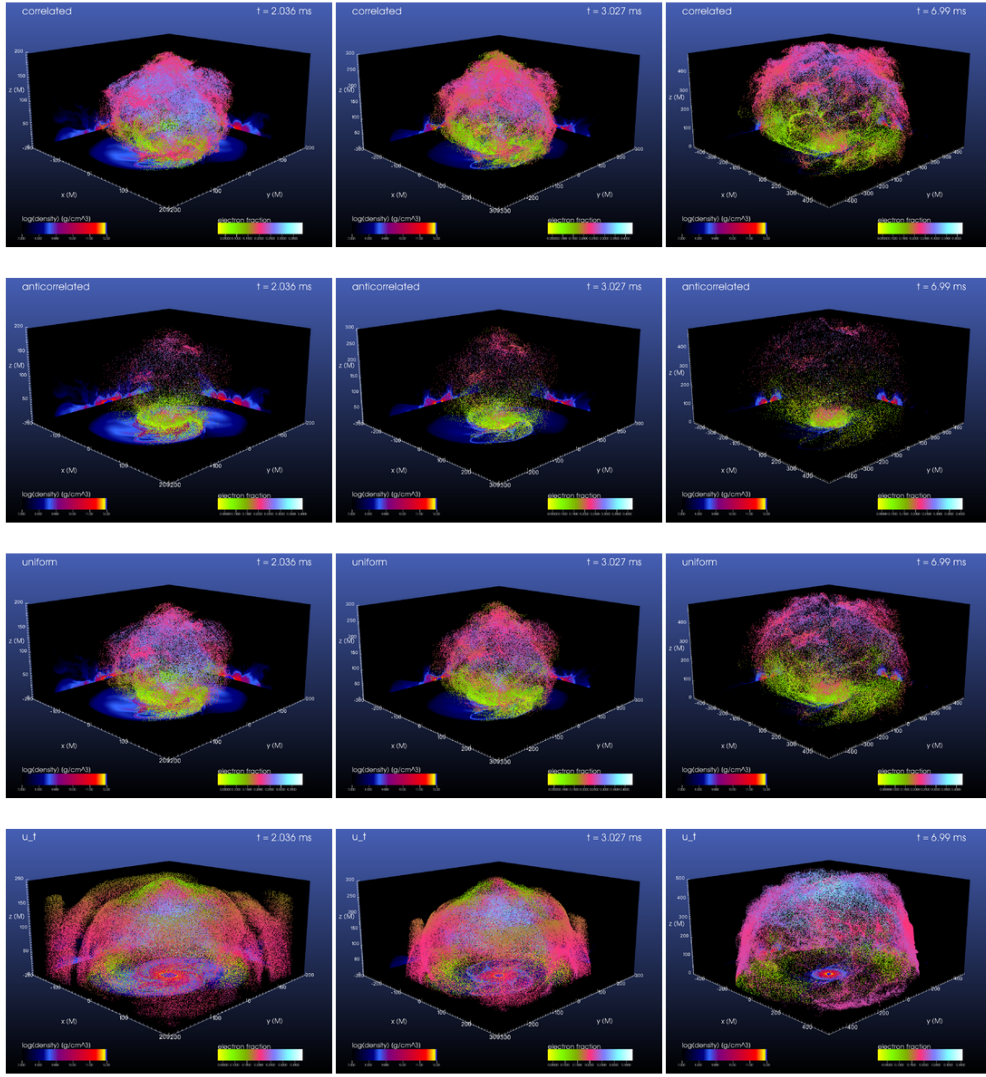


**Figure 4.** Visualisation of the tracers for four different placement schemes (top to bottom) at three different times (left to right). From top to bottom: “correlated”, “anticorrelated”, “uniform”, and “unbound”. From left to right to  $\sim 2, 3, 7$  ms after merger. On the  $(x, y)$ ,  $(y, z)$ , and  $(x, z)$  planes are shown the values of the rest-mass density using the colourbar in the left lower corner. A colourbar on the right lower corner is also used to visualise the electron fraction  $Y_e$  of the fluid elements hosting the tracers.

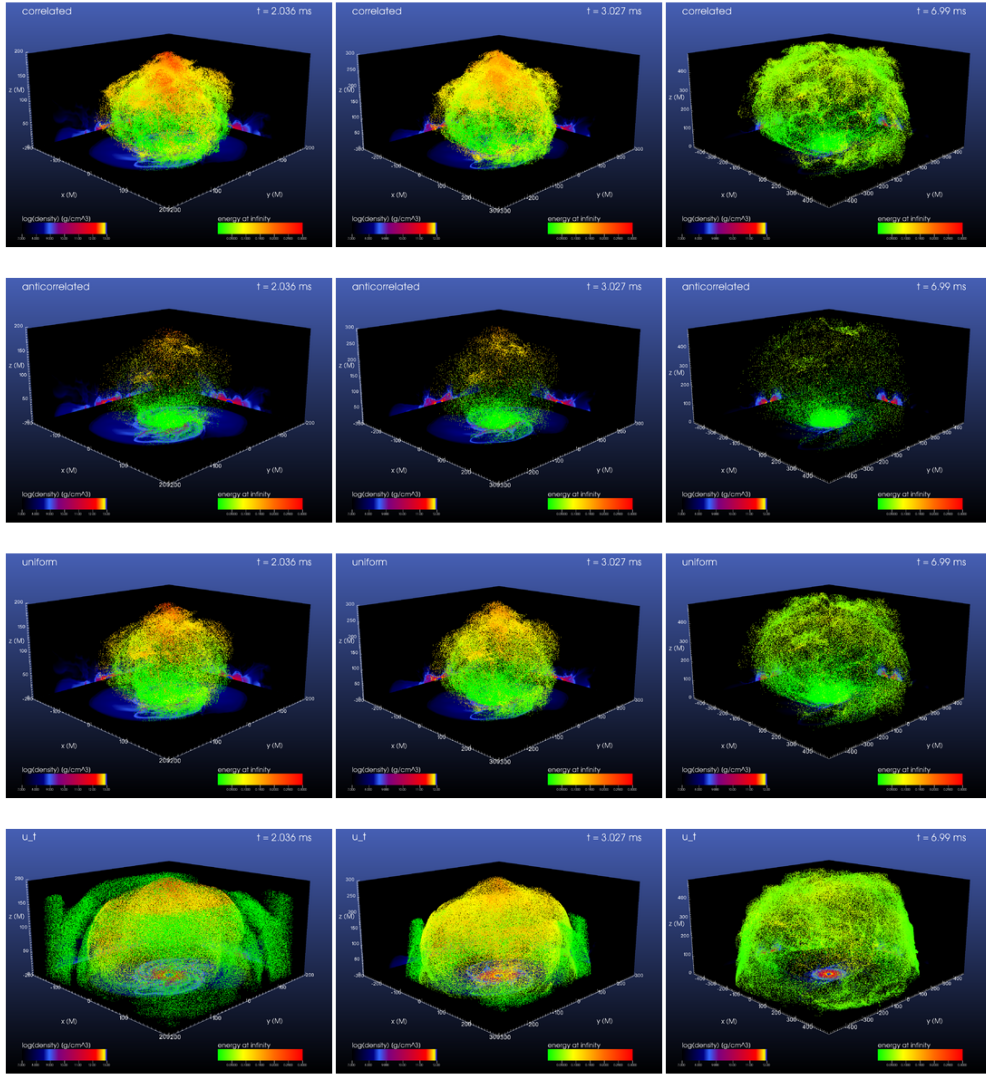


**Figure 5.** Visualisation of the tracers for four different placement schemes (top to bottom) at three different times (left to right). From top to bottom: “correlated”, “anticorrelated”, “uniform”, and “unbound”. From left to right to  $\sim 2, 3, 7$  ms after merger. On the  $(x, y)$ ,  $(y, z)$ , and  $(x, z)$  planes are shown the values of the rest-mass density using the colourbar on the right lower corner. A colourbar on the left lower corner is also used to visualise the kinetic energy at infinity,  $K := -u_t - 1$ .

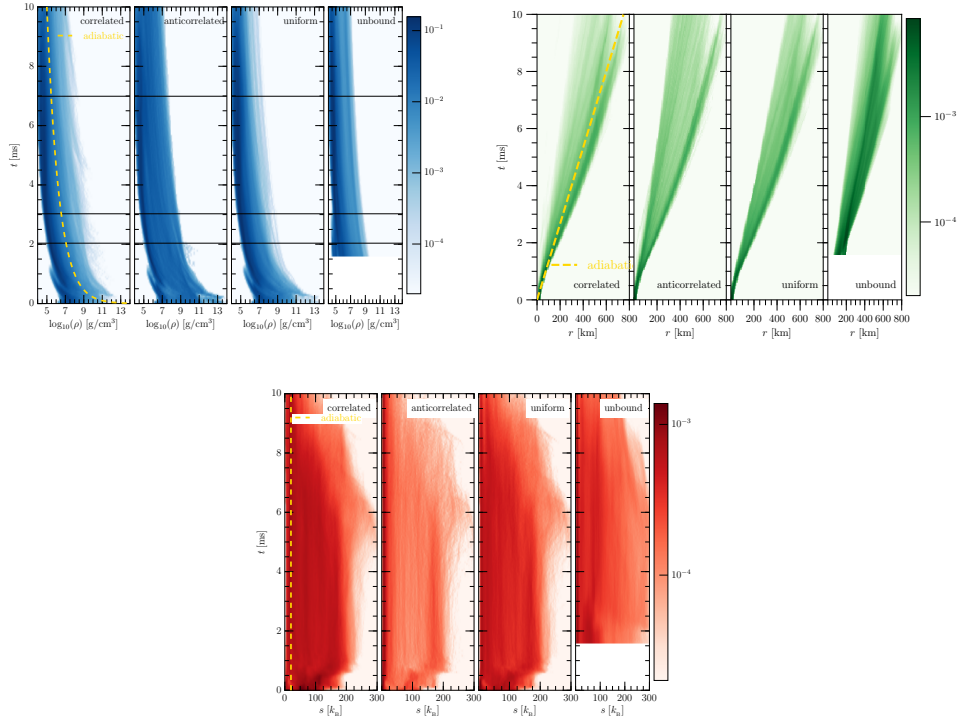
high rest-mass densities and oversampled those at high rest-mass density. Not surprisingly, the “uniform” tracers strikes a place between the two (third row). Finally, the case of “unbound” tracers (fourth row) shows a very different structure, where it is possible to clearly distinguish the different “waves” of matter ejected dynamically (left and central columns) and where an almost spherically “dome” develops over the BMP product and which is not present in the other placements. Note that this should not be interpreted as an indication that the mass outflow is spherically symmetric as the tracers in this case are not a faithful description of the rest-mass density. Indeed, when using the colourbar to track the actual rest-mass density, it is possible to note that high rest-mass density material (coloured red) is ejected mostly near the equatorial plane, while low rest-mass density material (coloured blue) is ejected at higher latitudes. Hence, the ejected material has a strong angular dependence. This is particularly important in view of the previous studies of nucleosynthesis with tracers carried out in Ref. [37], where the tracers were analysed only on the  $(x, y)$ ,  $(y, z)$ , and  $(x, z)$  planes, and of the fact that the angular dependence of the tracers can change the potential observed properties (see Refs. [27, 39] for a discussion). The snapshots in Fig. 3 demonstrate that there is significant material that lies outside these planes; indeed, as we will further discuss in Sec. 3.4, about 50 % of the mass ejected lies within 10 degrees of the orbital plane, while the remaining 50 % occurs at higher angles from the equator.

Figure 4 is similar to Fig. 3 but we use the colourbar to represent the value of the electron fraction  $Y_e$  carried by the various tracers. In all placements, we see a similar distribution of the electron fraction, with low  $Y_e$  values near the equator and increasingly high values near the poles. For all distributions, this increase in  $Y_e$  is correlated with a decrease in the rest-mass density. Thus despite having potentially high- $Y_e$  ejecta in the polar regions, it is associated with only a modest amount of ejected matter. Overall, the snapshots indicate that there will be a strong angular dependence of the r-process nucleosynthesis; a detailed discussion of this will be presented in an accompanying paper [55]. Finally, Fig. 5 is similar to the two previous ones but refers now to the kinetic energy at infinity, i.e.,  $K := -u_t - 1$ , so that  $K \geq 0$  corresponds to  $u_t \leq -1$ . Clearly, all snapshots show that, independently of the placement criterion chosen, the material near the equator is just unbound, but, as the latitude increases, the material becomes more unbound, increasing to a maximum at the poles. Similarly, at late times, we can see that all the high-energy material has already been ejected in the violent dynamics accompanying the early postmerger and that most values of  $K$  are close to zero. In summary, when analysed in a combined manner the three-dimensional dynamics of the unbound tracers shown in Figs. 3–5 reveals that the ejected matter near the poles has lower densities, but larger values of electron fraction and kinetic energy, and such a picture has implications for the detection and observation of kilonova [55].

### 3.3. Distribution dynamics of unbound tracers

A key assumption often made in studying the outflow material in r-process nucleosynthesis and in kilonova modelling [12, 52], is that the unbound material is expanding adiabatically, i.e., that the internal energy remains constant. In addition, the material is assumed to expand radially, so that the rest-mass density decreases in time as  $\sim t^{-3}$ . While all reasonable, our use of tracers allows us now to test these assumptions. We do this by reporting in Fig. 6 the time evolution of the distribution functions of representative quantities, i.e., the rest-mass density, the radial position, the specific entropy<sup>||</sup>. In these plots, the worldlines of the various tracers are marked with small dots whose colour marks the corresponding fraction; as a result,

<sup>||</sup> A diagram showing the evolution of the distribution function of the radial position of the various tracers effectively represents a spacetime diagram, thus offering the opportunity to visualise the (radial) worldlines of the tracers.



**Figure 6.** Evolution of the distribution functions for three representative quantities: the rest-mass density, the radial position and the specific entropy. From left to right are the “correlated”, “anticorrelated”, “uniform”, and “unbound” placements. The yellow lines represent the adiabatic expansion for each of the plotted quantities. Note that the “unbound” placement starts 1.8 ms after the merger. Horizontal black lines correspond to the times shown in Figs. 3–5.

a dark/light trajectory will indicate that a large/small number of tracers with the corresponding quantity having the reported values at a given time.

In the top left panel of Fig. 6 we show the evolution diagram of the evolution of rest-mass density, with the dashed-gold curve representing adiabatic expansion,  $\rho \sim t^{-3}$ . The four sub-panels distinguishing the various criteria adopted for the initial placement, while the horizontal black lines correspond to the times shown in Figs. 3–5. In all cases, the general trend of the adiabatic expansion can be seen very clearly and involves both tracers with high rest-mass density and tracers with low rest-mass density. However, it is important to note that while the general trend is for an adiabatic expansion, not all tracers follow this behaviour. For example, in the case of “correlated” tracers, the panel shows that there is a small fraction of tracers (light blue) corresponding to higher rest-mass densities that does not always follow the adiabatic expansion prior. Another feature is the number of tracers that reach close to atmospheric values and that eventually represents a large fraction of the total number (dark blue). In all placements considered there is a clear gradient of colours with increasing rest-mass density. An exception to this behaviour is offered by the case of “anticorrelated” tracers, where the fraction gradient is not as strong. This is a manifestation of the initial placement scheme: there are more tracers at high rest-mass densities and of those that become unbound, they represent a significant fraction of the unbound material.

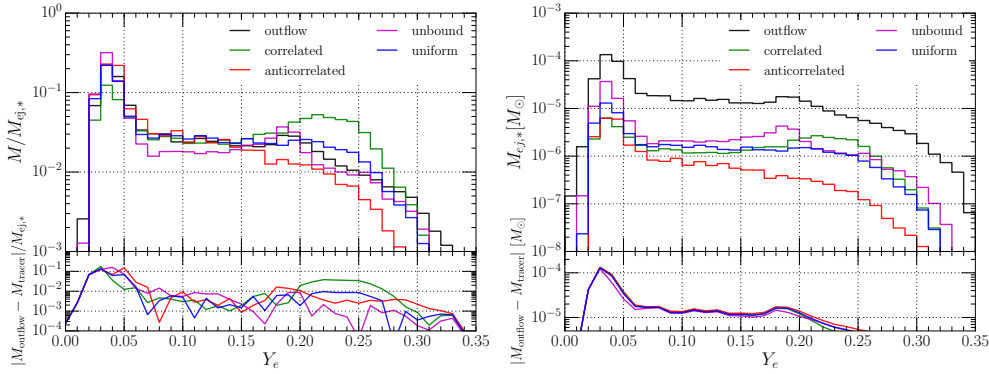


**Figure 7.** *Left panel:* Comparison between the distributions in electron fraction as computed with the tracer mass-fluxes through the surface at  $200 M_{\odot}$  as computed with the different placement schemes (coloured lines) and the outflow (black line). Because the ejected masses are different in the various cases, all curves have been normalised to the masses of their respective total values. Shown in the bottom part is the relative error, which is smaller for the uniform distribution placement. *Right panel:* The same as in the left but when the distributions are absolute and not normalised.

Similarly, in the top right panel of Fig. 6 we show a standard spacetime diagram of the radial distance from the origin of the tracers; note that the “unbound” placement starts 1.8 ms after the merger. In the adiabatic approximation, the expansion radius  $r$  should scale linearly with time, i.e.,  $r \sim t$ , and the figure shows clearly that most tracers do follow a very close to radial ejection. In addition, we can see the wide distribution of the tracers. Our domain is approximately 750 km wide from the origin in each direction and the tracers have a radial distance ranging from 300 km up to 800 km at any given time. This spatial distribution has been discussed in terms of the neutrino-drive wind ejecta [27] but has not been explored in the dynamic ejecta case in general relativity.

Finally, in the bottom panel of Fig. 6 we show the evolution of the distribution function for the specific entropy, such that an adiabatic expansion would simply be represented by a vertical line for each tracer. The panel allows us to clearly note that indeed many of the tracers obey this adiabatic expansion, but not all. For example, it is clear that at high entropies the tracers do not expand adiabatically and that tracers can actually increase their entropy, for instance as a result of additional shocks with the outgoing matter. Hence, this panel illustrates that the assumptions made that the ejected matter follows an adiabatic flow is a very valid approximation for much of the unbound material, but in order to have the most robust input data for the nuclear network, one needs to have the full history of the fluid element. This is in contrast with the analysis of [18], where the unbound material was expanded adiabatically from the surface of the outflow sphere.

### 3.4. Tracer and fluid information

In the previous sections we have illustrated how different choices for the placement of the tracers can lead to different dynamics of the tracers and hence to different measurable quantities. We now address the issue of which of these possible choices should be the recommended one in numerical simulations in order to most accurately represent the underlying fluid. In particular, to determine the efficacy of the different placements, we have compared the tracer distributions of the most important thermodynamical and physical



quantities, i.e., electron fraction, entropy, energy at infinity, angular distribution of the mass flux, with the corresponding distributions from the underlying fluid evolution; hereafter we refer to the latter as the (fluid) “outflow”. As in the previous discussions, we compute our distributions in terms of the fluxes across a spherical detector at  $200M_{\odot}$  from the origin and consider only material that is unbound according to the geodesic criterion.

Perhaps the most important quantity of all thermodynamical quantities is the electron fraction  $Y_e$ , which measures how neutron rich the material is. The value of the electron fraction relates to which r-process elements are created and what kind of kilonova is produced. For these reasons, it is the quantity which we will use to determine which placement best matches that of the underlying fluid. In Fig. 7 we plot the distributions of the electron fraction using the different placement prescriptions (marked with lines of different colour) along with the distribution obtained with the fluid “outflow” (black). In the bottom panel we also plot the error between each of the tracer prescriptions with that of the “outflow”. In the left panel, in particular, all curves are normalised to the amount of rest-mass ejected in the various cases,  $M_{\text{ej},*}$ , so that the integral of the various distributions is unity. In the right panel of Fig. 7 such a normalisation is not used and the distributions refer to the absolute amount of ejected matter for the different distributions.

Overall, the fluid-outflow distribution (black solid line) shows that the electron fraction has a main peak at  $Y_e \sim 0.04$  and a secondary one at  $Y_e \sim 0.19$ . Concentrating on the left panel, we clearly note that the “anticorrelated” and “uniform” placements both give the correct value for the  $Y_e \sim 0.04$  peak with a relative error of  $\sim 10^{-2}$  and  $10^{-3}$  respectively. On the other hand, the “unbound” ( $u_t$ ) and the “correlated” placements over- and underestimate it respectively by roughly the same amount of  $10^{-1}$ . In particular, for the secondary peak, the “correlated” placement overestimates the peak significantly with an error of about 50%; a much better agreement is obtained with the “unbound” and “uniform” distributions, with errors that are of a few percent only. In the intermediate electron-fraction range, i.e., for  $0.04 \lesssim Y_e \lesssim 0.19$ , all placements provide an accurate description, with the only exception of the “unbound” placement, which tends to underestimate the underlying fluid. Hence, all things considered, we can conclude that the initial tracer placement that provides the best match with the consistent fluid evolution is the “uniform” distribution.

This is a somewhat surprising result as one would have naively expected that the “correlated” placement would have provided a more faithful representation of the fluid dynamics. In order to appreciate why this is not the case, we report in Fig. 8 the initial distributions in rest-mass density of the tracers (light-yellow shade) and the corresponding distributions when the tracers cross the  $200M_{\odot}$  surface. In particular, the comparison presented in the top left panel allows us to appreciate that initially there were significantly more tracers at low rest-mass densities for the “correlated” placement, so that we are effectively oversampling at lower rest-mass densities and, consequently, undersampling at high rest-mass densities. Indeed, there are no tracers that come from above  $\sim 10^{12} \text{ g/cm}^3$  while almost all tracers below  $10^9 \text{ g/cm}^3$  become unbound. Because the lower densities also have higher values of  $Y_e$ , the “correlated” placement de-facto leads to an oversampling around  $Y_e \sim 0.18$  (hence the second broad peak in the distribution) and to an undersampling at  $Y_e \sim 0.05$  (hence the smaller first peak in the distribution). Not surprisingly, the “anticorrelated” placement suffers of the opposite problem. It undersamples at lower rest-mass densities resulting in there being fewer tracers with large values of  $Y_e$ . More precisely, the top right panel of Fig. 8 shows that there is a significant number of tracers above  $10^{12} \text{ g/cm}^3$ , which have low values of  $Y_e$ , thus yield a good agreement with the first peak. However, at lower rest-mass densities, a higher percentage of tracers that become unbound come from lower densities and hence we are effectively and significantly undersampling matter at low densities.

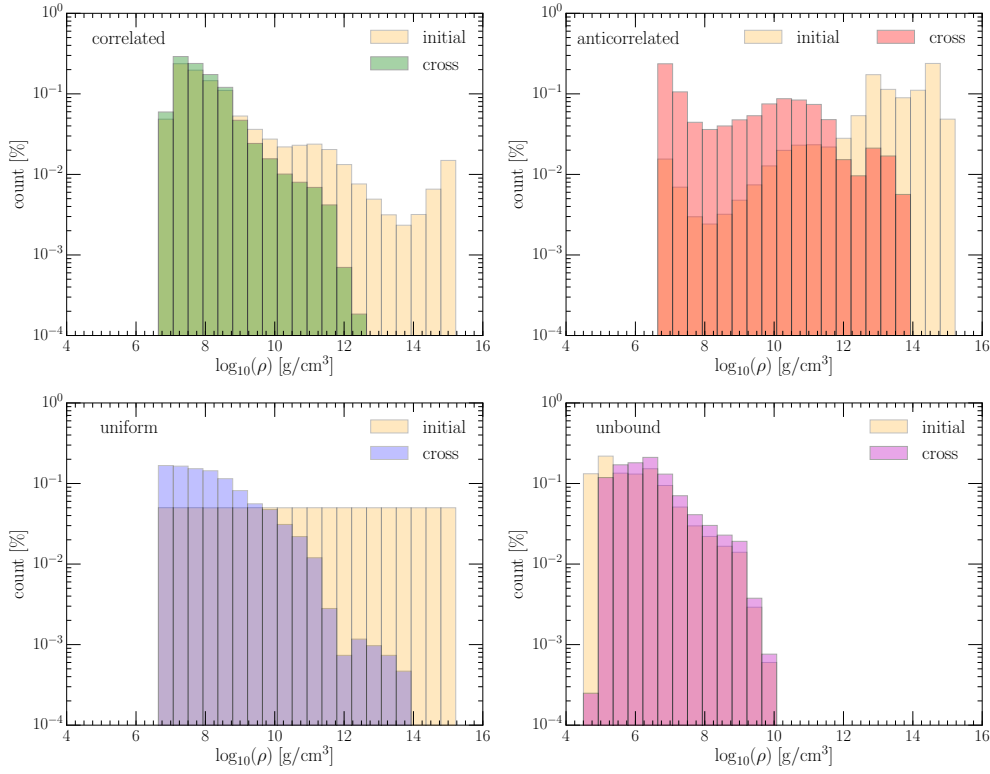


**Figure 8.** Distributions in rest-mass density of the tracers (light-yellow shade) and the corresponding distributions when the tracers cross the  $200 M_{\odot}$  surface. Shown from left to right are the distributions corresponding to the “correlated”, “anticorrelated”, “uniform”, and “unbound”.

For example, only about 1% of the initial tracers were placed at the lowest initial rest-mass density of  $\sim 10^7 \text{ g/cm}^3$ , but almost 20% of the tracers that are unbound come from these rest-mass densities. Examining the bottom left panel of Fig. 8 we can also appreciate that the “uniform” placement distribution is, in a sense, the average of the above two placements. It uniformly samples from all densities and hence has no oversampling or undersampling at high and low rest-mass densities. As shown in Fig. 8 tracers that are initially at  $10^{14} \text{ g/cm}^3$  become unbound, as in the case of the “anticorrelated” placement; at the same time, the tracers at low rest-mass densities are unbound, thus making the “uniform” placement be the most effective one, besides being also the simplest to implement.

When considering the “unbound” placement, the bottom right panel of Fig. 8 shows that there is a remarkably good match between the initial distribution of the placed tracers and the distribution at detector crossing, especially for medium and high rest-mass densities. Yet, while such a placement nicely reproduces the counts at the two peaks in electron fraction, it also fails to capture the values between the two peaks, as shown in the left panel of Fig. 7. This is most likely due to the fact that this placement completely misses some of the material that the other tracer placements instead capture. In particular, it undersamples the material that is at low rest-mass density and that can become unbound as a result of shock heating. Hence, the behaviour in Figs. 7 and 8 highlights a potential drawback of the “unbound” placement procedure, that one may naively assume to be particularly good. This placement, in fact, while

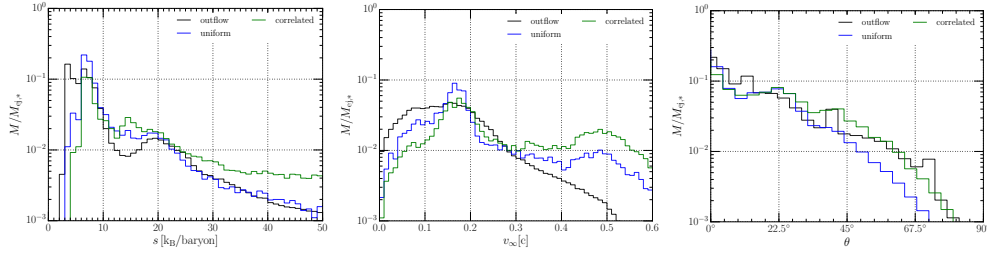


**Figure 9.** Comparison between the distributions in electron fraction as computed with the tracer mass-fluxes through the surface at  $200 M_{\odot}$  as computed with the different placement schemes (coloured lines) and the outflow (black line). The quantities considered are: the entropy, the velocity at infinity, and the angular distribution; all curves have been normalised to the corresponding total ejected masses (cf. Fig. 7).

it can nicely sample the unbound material, only captures material that is unbound at a given moment and neglects any material that might become unbound and that has not yet become unbound, most notably, the very low rest-mass density material.

Finally, in Fig. 9 we compare other thermodynamical and physical quantities similar the one presented in Fig. 7. These three quantities are: the specific entropy (left), the velocity at infinity (middle), and the angular distribution (right). Here, we concentrate on a comparison between the fluid outflow (black line), the “uniform” distribution placement (blue line), and the “correlated” placement (green line). Note how the specific-entropy distributions are all rather similar, although the “uniform” placement undersamples at the first peak and does not show a local minimum at around  $15 k_{\text{B}}/\text{baryon}$ . The velocity at infinity is another measure of the  $u_t$  and here we do not see great agreement at higher values. These higher values correspond to the more energetic tracers, thus indicating that both the “uniform” and the “correlated” placement tend to oversample the highly energetic material. Similar considerations apply to the angular distribution of the ejected, where the two placement schemes show rather similar results, both in agreement with the fluid evolution, even though the tracer mass flux shows slightly more mass at the higher angles. Interestingly, the tracer evolution is also able to reproduce the local maximum at  $\sim 45^\circ$  which a numerical artefact of the Cartesian grid and was first mentioned in Ref. [18].

*In conclusion, we have found that out of the initial tracer placements considered, the “uniform” placement results in the best agreement with the underlying fluid based on a comparison with the electron fraction. This is due to the “uniform” method sampling both high and low rest-mass densities uniformly, avoiding over- or undersampling in these regimes.*

#### 4. Tracing bound material

We conclude our discussion on the use of tracers by considering the case in which they are employed to describe the dynamics of matter that is gravitationally *bound*. Despite already having a complete description of the fluid dynamics as measured by Eulerian observers, there are a number of reasons why using tracers could be a powerful tool. The most important of such reasons is that tracers following bound fluid elements allow us to disentangle the local dynamics of the fluid from the global one. Because both of these dynamics can be complex and operate on different timescales, having the possibility of setting them apart is quite valuable to interpret the results of simulations. There are several examples of the successful use of tracers in bound material (see, e.g., the interesting analysis of precessing

and tilted disk accretion in Ref. [73]), but we will here concentrate on the dynamics of the HMNS produced by the merger of a binary system of neutron stars, following the discussion already presented in Ref. [56].

More specifically, we are interested here in studying the rotational properties of the HMNS produced by the merger of a binary system of neutron stars. The dynamics of this object, which is metastable and doomed to collapse to a black hole because its mass is above that sustainable through uniform rotation, is made complicated by the fact that it is subject to violent oscillations and, at the same time, it is subject to a bar mode deformation that leads to a copious emission of gravitational waves. Hence, a deeper understanding of the distribution of angular momentum and angular velocity can help in determining under what conditions the HMNS will collapse to a black hole. It is therefore useful to study the angular velocity of the fluid, which we measure as

$$\Omega := \alpha v^\phi - \beta^\phi, \quad (11)$$

where  $\phi$  refers to the azimuthal direction (see [56] for a more detailed discussion). Hereafter we will concentrate on the HMNS produced when two identical neutron stars with a (gravitational) mass of  $1.35 M_\odot$  and described by the hot DD2 EOS, but a much large sample of binaries has been explored in Ref. [56].

#### 4.1. Initial placement

Selecting the optimal initial placement when studying bound flow is much less problematic since we are not trying to accurately capture the statistics of the underlying fluid. Indeed, so long as it is clear as to what region of the fluid we are interested in, then placing tracers is mostly a matter of deciding a good time for the seeding and employing a sufficiently large number of tracers so that all parts of the flow are properly represented. Because we are interested in tracking the motion in the core of the HMNS, it is straightforward to set the time of the merger as the time for the tracer seeding. Furthermore, for the spatial placement we do not follow any probability distribution associated with the rest-mass density but simply place a single tracer in each of the fluid cells that we mark to be within a certain region of the computational domain, namely, the core of the HMNS. In practice, using  $\sim 10^5$  tracers is sufficient to ensure that every cell within the core had a tracer in it. As in Ref. [56], of the  $10^5$  initially placed tracers, approximately 6000 remained on the  $(x, y)$  plane, thus allowing us to study the fine details of the fluid motion on this plane.

#### 4.2. Dynamics of the HMNS

In Fig. 10 we plot a representative time, approximately  $\sim 5.5$  ms after the merger, of the evolution of the rest-mass density (left) and the angular velocity (right). In the top panel we chose the frame of an observer at infinity (Eulerian), while in the bottom we chose the “corotating frame”<sup>¶</sup>. The tracers plotted here are just a representative of the  $\sim 6000$  tracers that remain in the  $(x, y)$  plane throughout the entire evolution. For each tracer we use a small filled circle to report the position at the given time, and use solid lines of decreasing size the join the position at two previous times separated by  $\sim 0.3$  ms. The “tails” that are produced in this manner provide a simple way to visualise the tracer streamlines and hence the evolution of the fluid as it rotates around the core. Also, the number of tracers is sufficient to completely cover the core and all key features are represented by numerous tracers, however

<sup>¶</sup> We recall that the corotating frame is a frame rotating at a frequency that is half of the instantaneous gravitational-wave frequency,  $\Omega_{\text{GW}}$ . Here  $\Omega_{\text{GW}}/2 = 1291$  Hz.

only representative ones are plotted to illustrate the rich evolution of the feature that is difficult to observe without the streamlines.

The tracers immediately clarify and illustrate the evolution of the fluid. As seen in the bottom left panel of Fig. 10, the underlying rest-mass density clearly exhibits an  $l = m = 2$  deformation; however, because this deformation is not stationary in an Eulerian frame, it is difficult to discern the motion of the fluid, as can be observed by the tracers in the top left panel. With tracers, on the other hand, we can clearly see that there is a central bar around which the tracers flow, but beside this bar there are two vortices that trap fluid (bottom of Fig. 10). This pattern can be more clearly seen in the angular velocity, where these side vortices have higher angular velocity compared with the central bar. Additionally, the tracers illustrate further the structure of the angular velocity distribution. In particular, in the vortices the fluid is revolving faster than the corotating frequency – and hence move counterclockwise – while other tracers either corotate – hence they appear not to move – or rotate more slowly than the corotation frequency – and hence move clockwise. The combined use of tracers and the corotating frame demonstrate the ability to visualise features of the core that are otherwise difficult to visualise.

Another advantage of the tracers is that they allow the computation of quantities along their streamlines and, in particular, of quantities that are expected to be conserved if the fluid is perfect and the flow is isentropic, e.g., the Bernoulli constant. Keeping track of such quantities can be extremely useful to explain a behaviour which would otherwise appear puzzling. For instance, in Ref. [56] it was proposed that the dependence of the angular velocity depends inversely on the rest-mass density, through the Bernoulli constant. This conjecture explains why the rest-mass density and angular velocity profiles have a clear 90 degree phase difference (cf. left and right panels of Fig. 10). This assertion, however, is difficult to verify without tracers and the streamlines they can provide.

We recall that in relativistic hydrodynamics and for a perfect fluid with four-velocity  $u$ , the quantity  $h(u \cdot \xi)$  is Lie-dragged along  $u$  [59]

$$L_u(h u \cdot \xi) = 0, \quad (12)$$

where  $h := (e + p)/\rho$  is the specific enthalpy,  $e := \rho(1 + \epsilon)$  is the total energy density, and  $\xi$  is a Killing vector of the spacetime and also a generator of the symmetry obeyed by the fluid. If spacetime admits a timelike Killing vector so that the fluid motion is stationary, then the quantity  $\mathcal{B} := hu_t$  is a constant of the fluid. In its classical limit, Eq. (12) becomes

$$\left(1 + \epsilon + \frac{p}{\rho}\right) \left(1 + \phi + \frac{1}{2}\bar{v}^2\right) = \text{const.}, \quad (13)$$

where  $\phi$  is the gravitational potential and  $v$  is the local fluid velocity. When neglecting higher-order terms and taking the gravitational potential to be independent of time and essentially constant across the HMNS, expression (13) further reduces to

$$\left(\frac{1}{2}\bar{v}^2 + \epsilon + \frac{p}{\rho}\right) = \text{const.}, \quad (14)$$

which coincides with the classical expression for the Bernoulli constant [59]. Clearly, the post-merger phase of a BNS merger does not satisfy the timelike Killing vector assumption, but we can still use tracer particles to appreciate how well the Bernoulli constant is conserved along streamlines.

Figure 11 provides a simple example of how the evolution of tracers allows one to quickly and simply perform the analysis of very precise regions of the fluid. In particular, the panels in Fig. 11 show the time evolution of several quantities relative to three tracers that have been chosen as representative of three areas of the HMNS: the inner core (i.e.,  $r \lesssim 4$  km),

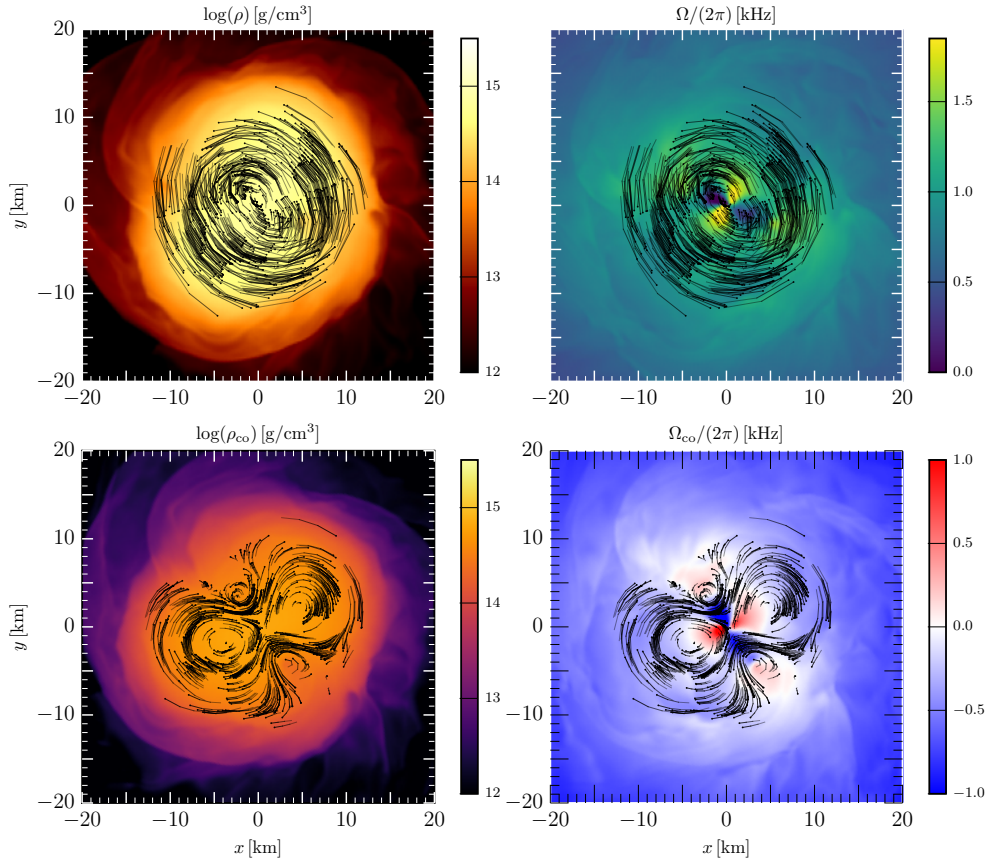


**Figure 10.** Distributions on the  $(x, y)$  plane of the rest-mass density (left panels), and of the angular velocity (right panels). The top panels are relative to the Eulerian frame at time  $t = 5.5$  ms, while the bottom panels refer to a corotating frame with angular velocity  $\Omega_{\text{co}} := \Omega - \Omega_{\text{GW}}/2$ , where  $\Omega_{\text{GW}} = 2582$  Hz is the instantaneous gravitational-wave frequency. Also shown are portions of the flowlines of several tracer particles that remain close to the  $(x, y)$  plane and for which we show only the final part of the flowlines (i.e., for the last  $\simeq 0.285$  ms), using small dots to indicate the particle position at the time indicated in the frame. In addition, the initial parts of the trajectories have increasing transparency so as to highlight the final part of the trajectories.

the middle core (i.e.,  $4 \lesssim r \lesssim 6$  km), and the outer core (i.e.,  $6 \lesssim r \lesssim 8$  km). The top panels, in particular, show the evolution of the specific entropy which, during the violent post-merger phase, undergoes a sudden jump due to heating, but quickly settles to become approximately constant. The bottom panels, instead, shows the evolution of the Bernoulli constant in light blue.

In essence, Fig. 11 shows that even though the post-merger phase does not exhibit a timelike Killing vector, the Bernoulli constant stays roughly constant across the interior of the HMNS. This constant behaviour can be used to explain the phase difference observed in Ref. [56] where the rotation-profile is out-of-phase with the barmode from the rest-mass density. In fact, while the values of (14) are strictly not constant in time (especially in the grey-shaded areas), they also do not vary significantly around the initial values. More importantly, there is a phase opposition in the evolution of the kinetic term  $v^2/2$  and of the pressure term

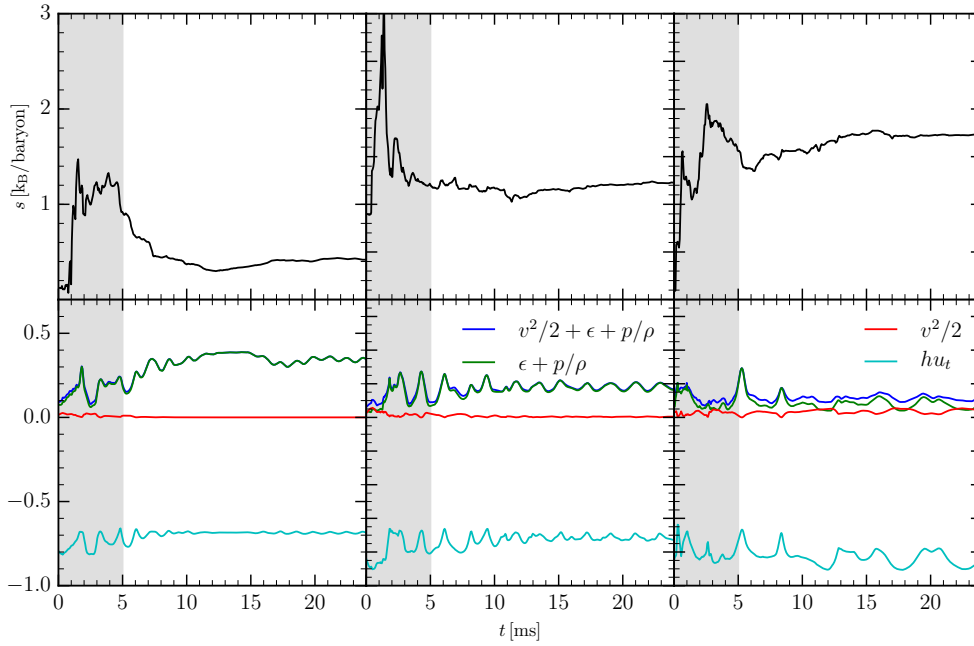


**Figure 11.** *Top panels:* Evolution of the entropy for tracers in the HMNS that are eventually either in the inner core (i.e.,  $r \lesssim 4$  km; left panel), in the middle core (i.e.,  $4 \lesssim r \lesssim 6$  km; middle panel), or in the outer core (i.e.,  $6 \lesssim r \lesssim 8$  km; right panel). *Bottom panels:* evolution of the Bernoulli constant  $hu_t$  (light blue line), the classical Bernoulli constant  $v^2/2 + \epsilon + p/\rho$  (blue line) and its main contributions:  $\epsilon + p/\rho$  (green line) and the kinetic term  $v^2/2$  (red line). The grey-shaded area refers to the postmerger transient when the HMNS is far from an equilibrium.

$\epsilon + p/\rho$ , so that large values of the former correspond to low values of the latter and vice versa, thus providing a simple and intuitive explanation for the phase difference in the two quantities.

## 5. Conclusions

Accurate numerical simulations of the merger of binary systems of neutron stars are becoming increasingly more important as the detection of gravitational waves from such systems is expected within the next few years and is likely to bear a wealth of information in physics and astrophysics. A particularly important aspect of this process that has recently received considerable attention, is the ejection of matter from the merger, which is expected to be well suited for r-process nucleosynthesis [11–18]. Because it naturally produces neutron-rich material, the merger of BNSs could represent the astrophysical site behind the origin of the heavy elements in our universe. A number of numerical simulations, in fact, have recently demonstrated that BNS mergers can provide a contribution to the chemical abundances of heavy elements that is several orders of magnitude larger than that given by supernovae, whose ejected material is not enough neutron-rich to match with observed values in the solar system. In addition, this ejected r-process material will likely produce an electromagnetic counterpart known as a kilonova that can additionally provide a wealth of information about the nuclear physics of the r-process.

However, due to the long timescales required for the nuclear-reaction networks, present numerical-relativity simulations are unable to take directly into account the complex nuclear reactions, which must therefore be analysed in a post-processing step. It follows that there is a need for robust and accurate methods that can be combined with the nuclear-reaction networks to produce abundance patterns from merger simulations. Tracers, that is, massless particles that are passively advected, are an effective way of recording the thermodynamical history of the fluid in grid-based codes and as such have been employed by a number of recent simulations of merging neutron-star binaries. However, while not particularly expensive to compute, the use of tracers requires a judicious initial placement, both in time and space, and especially if the portion of the fluid one is interested in is the one that is gravitationally unbound. This is because different placements can potentially lead to different physical observables and hence to different physical conclusions on the properties of the underlying fluid.

In this paper we have investigated the efficacy of how well the tracers can match the underlying fluid by directly comparing results from the fluid itself. More specifically, we have evaluated four different placement schemes that could be used to initially distribute the tracers and how well their predictions match those obtained when using information from the actual fluid flow. The four schemes considered are built by constructing distribution functions of the tracers that are either directly *correlated* with the rest-mass density distribution, or *anti-correlated*, or *uniformly* distributed, or, as a final case, independent on the rest-mass density and related instead to the portion of fluid that is *unbound*. Countering our naive expectations that placements that are correlated with the rest-mass density distribution or that follow the fluid that is marked unbound, we have found that the most effective method is to *uniformly* sample across the rest-mass density distribution as this leads to the closest matching with the unbound material that is flowing through a detector. This match has been measured in terms of a large number of physical quantities, such as the unbound rest-mass, the distributions of electron fraction, specific entropy and kinetic energy. Interestingly, the most important reason why a uniform distribution represents the optimal one is that it has the merit of sampling sufficiently from both the high and low rest-mass density regions that are ejected during the merger. Other methods, in fact, tend to either underestimate or overestimate the contributions coming from certain regions of the fluid.

In addition, tracers can be also used for a fine analysis of the motion of the fluid in regions that are highly complex, providing information on the properties of the fluid and on the quantities that should be conserved along streamlines if the flow is adiabatic. We have illustrated this by considering the motion of tracers in the core of an HMNS produced in the merger of a BNS system. We have shown that tracers provide a novel way to show the evolution of the fluid and display features that are otherwise difficult to observe and analyse. As a representative example, we have shown that the fluid vortices can form in the HMNS where matter is locally trapped and that these vortices are located in regions of low rest-mass density and high fluid velocity, as expected from the conservation of the Bernoulli constant. In a forthcoming work, we use the results discussed here to investigate a wide range of EOS and masses and the nucleosynthesis produced from the tracers ejected during the dynamical-ejection phase. Additionally, we will use the tracer data as input for radiative-transfer models to calculate the light curves resulting from the corresponding kilonova [55].

### Acknowledgements

It is a pleasure to thank Filippo Galeazzi, Matthias Hanauske, Bruno Mundim, David Radice for useful discussions. This research is supported in part by the ERC synergy



grant “BlackHoleCam: Imaging the Event Horizon of Black Holes” (Grant No. 610058), by “NewCompStar”, COST Action MP1304, by the LOEWE-Program in the Helmholtz International Center (HIC) for FAIR, and by the European Union’s Horizon 2020 Research and Innovation Programme (Grant 671698, call FETHPC-1-2014, project ExaHyPE). LB is supported by HIC for FAIR and the graduate school HGS-HIRE. The simulations were performed on the SuperMUC cluster at the LRZ in Garching, on the LOEWE cluster in CSC in Frankfurt, and on the HazelHen cluster at the HLRS in Stuttgart.

- [1] The LIGO Scientific Collaboration and the Virgo Collaboration 2016 *Phys. Rev. Lett.* **116** 061102 (Preprint [1602.03837](#))
- [2] Accadia T *et al.* 2011 *Class. Quantum Grav.* **28** 114002
- [3] Kuroda K and LCGT Collaboration 2010 *Class. Quantum Grav.* **27** 084004
- [4] Punturo M *et al.* 2010 *Class. Quantum Grav.* **27** 084007
- [5] Narayan R, Paczynski B and Piran T 1992 *Astrophysical Journal, Letters* **395** L83–L86 (Preprint [astro-ph/9204001](#))
- [6] Eichler D, Livio M, Piran T and Schramm D N 1989 *Nature* **340** 126–128
- [7] Rezzolla L, Giacomazzo B, Baiotti L, Granot J, Kouveliotou C and Aloy M A 2011 *Astrophys. J. Letters* **732** L6 (Preprint [1101.4298](#))
- [8] Bartos I, Brady P and Marka S 2013 *Class. Quant. Grav.* **30** 123001 (Preprint [1212.2289](#))
- [9] Berger E 2014 *Annual Review of Astron. and Astrophys.* **52** 43–105 (Preprint [1311.2603](#))
- [10] Baiotti L and Rezzolla L 2017 *Rept. Prog. Phys.* **80** 096901 (Preprint [1607.03540](#))
- [11] Lattimer J M and Schramm D N 1974 *Astrophysical Journal, Letters* **192** L145–L147
- [12] Li L X and Paczyński B 1998 *Astrophys. J.* **507** L59–L62 (Preprint [astro-ph/9807272](#))
- [13] Tanvir N R, Levan A J, Fruchter A S, Hjorth J, Hounsell R A, Wiersema K and Tunnicliffe R L 2013 *Nature* **500** 547–549 (Preprint [1306.4971](#))
- [14] Berger E, Fong W and Chornock R 2013 *Astrophys. J.* **774** L23 (Preprint [1306.3960](#))
- [15] Tanaka M and Hotokezaka K 2013 *Astrophys. J.* **775** 113 (Preprint [1306.3742](#))
- [16] Rosswog S, Korobkin O, Arcones A, Thielemann F K and Piran T 2014 *Mon. Not. R. Astron. Soc.* **439** 744–756 (Preprint [1307.2939](#))
- [17] Sekiguchi Y, Kiuchi K, Kyutoku K and Shibata M 2015 *Phys. Rev. D* **91** 064059 (Preprint [1502.06660](#))
- [18] Radice D, Galeazzi F, Lippuner J, Roberts L F, Ott C D and Rezzolla L 2016 *Mon. Not. R. Astron. Soc.* **460** 3255–3271 (Preprint [1601.02426](#))
- [19] Hotokezaka K, Kiuchi K, Kyutoku K, Okawa H, Sekiguchi Y i, Shibata M and Taniguchi K 2013 *Phys. Rev. D* **87** 024001 (Preprint [1212.0905](#))
- [20] Bauswein A, Goriely S and Janka H T 2013 *Astrophys. J.* **773** 78 (Preprint [1302.6530](#))
- [21] Dietrich T and Ujevic M 2017 *Classical and Quantum Gravity* **34** 105014 (Preprint [1612.03665](#))
- [22] Rosswog S 2005 *Astrophys. J.* **634** 1202 (Preprint [astro-ph/0508138](#))
- [23] Arnould M, Goriely S and Takahashi K 2007 *Physics Reports* **450** 97–213 (Preprint [0705.4512](#))
- [24] Metzger B D, Martínez-Pinedo G, Darbha S, Quataert E, Arcones A, Kasen D, Thomas R, Nugent P, Panov I V and Zinner N T 2010 *Mon. Not. R. Astron. Soc.* **406** 2650–2662 (Preprint [1001.5029](#))
- [25] Roberts L F, Kasen D, Lee W H and Ramirez-Ruiz E 2011 *Astrophys. J. Lett.* **736** L21 (Preprint [1104.5504](#))
- [26] Rosswog S 2015 *International Journal of Modern Physics D* **24** 1530012-52 (Preprint [1501.02081](#))
- [27] Martin D, Perego A, Arcones A, Korobkin O and Thielemann F K 2015 *ArXiv e-prints* (Preprint [1509.07628](#))
- [28] Arcones A and Thielemann F K 2013 *Journal of Physics G Nuclear Physics* **40** 013201 (Preprint [1207.2527](#))
- [29] Ji A P, Frebel A, Chiti A and Simon J D 2016 *Nature* **531** 610–613 (Preprint [1512.01558](#))
- [30] Tanaka M 2016 *Advances in Astronomy* **2016** 634197 (Preprint [1605.07235](#))
- [31] Metzger B D 2017 *Living Reviews in Relativity* **20** 3 (Preprint [1610.09381](#))
- [32] Rezzolla L, Baiotti L, Giacomazzo B, Link D and Font J A 2010 *Class. Quantum Grav.* **27** 114105 (Preprint [1001.3074](#))
- [33] Kyutoku K, Ioka K and Shibata M 2014 *Mon. Not. R. Astron.Soc.* **437** L6–L10 (Preprint [1209.5747](#))
- [34] Rosswog S 2013 *Royal Society of London Philosophical Transactions Series A* **371** 20272 (Preprint [1210.6549](#))
- [35] Dessart L, Ott C D, Burrows A, Rosswog S and Livne E 2009 *Astrophys. J.* **690** 1681–1705 (Preprint [0806.4380](#))
- [36] Perego A, Rosswog S, Cabezón R M, Korobkin O, Käppeli R, Arcones A and Liebendörfer M 2014 *Mon. Not. R. Astron. Soc.* **443** 3134–3156 (Preprint [1405.6730](#))
- [37] Wanajo S, Sekiguchi Y, Nishimura N, Kiuchi K, Kyutoku K and Shibata M 2014 *Astrophys. J.* **789** L39 (Preprint [1402.7317](#))

- [38] Just O, Bauswein A, Pulpillo R A, Goriely S and Janka H T 2015 *Mon. Not. R. Astron. Soc.* **448** 541–567 (Preprint [1406.2687](#))
- [39] Martin D, Perego A, Arcones A, Thielemann F K, Korobkin O and Rosswog S 2015 *Astrophys. J.* **813** 2 (Preprint [1506.05048](#))
- [40] Just O, Obergaulinger M, Janka H T, Bauswein A and Schwarz N 2016 *Astrophys. J. Lett.* **816** L30 (Preprint [1510.04288](#))
- [41] Sekiguchi Y, Kiuchi K, Kyutoku K, Shibata M and Taniguchi K 2016 *Phys. Rev. D* **93** 124046 (Preprint [1603.01918](#))
- [42] Murguia-Berthier A, Ramirez-Ruiz E, Montes G, De Colle F, Rezzolla L, Rosswog S, Takami K, Perego A and Lee W H 2017 *Astrophys. J. Lett.* **835** L34 (Preprint [1609.04828](#))
- [43] Shibata M, Suwa Y, Kiuchi K and Ioka K 2011 *Astrophys. J.* **734** L36 (Preprint [1105.3302](#))
- [44] Kiuchi K, Kyutoku K and Shibata M 2012 *Phys. Rev. D* **86** 064008 (Preprint [1207.6444](#))
- [45] Siegel D M, Ciolfi R and Rezzolla L 2014 *Astrophys. J.* **785** L6 (Preprint [1401.4544](#))
- [46] Rezzolla L and Kumar P 2015 *Astrophys. J.* **802** 95 (Preprint [1410.8560](#))
- [47] Ciolfi R and Siegel D M 2015 *Astrophys. J.* **798** L36 (Preprint [1411.2015](#))
- [48] Goriely S, Bauswein A and Janka H T 2011 *Astrophys. J.* **738** L32 (Preprint [1107.0899](#))
- [49] Kastaun W and Galeazzi F 2015 *Phys. Rev. D* **91** 064027 (Preprint [1411.7975](#))
- [50] Rosswog S, Piran T and Nakar E 2013 *Mon. Not. R. Astron. Soc.* **430** 2585–2604 (Preprint [1204.6240](#))
- [51] Piran T, Nakar E and Rosswog S 2013 *Mon. Not. R. Astron. Soc.* **430** 2121–2136 (Preprint [1204.6242](#))
- [52] Grossman D, Korobkin O, Rosswog S and Piran T 2014 *Mon. Not. R. Astron. Soc.* **439** 757–770 (Preprint [1307.2943](#))
- [53] Fernández R and Metzger B D 2013 *Mon. Not. R. Astron. Soc.* **435** 502–517 (Preprint [1304.6720](#))
- [54] Metzger B D, Bauswein A, Goriely S and Kasen D 2015 *Mon. Not. R. Astron. Soc.* **446** 1115–1120 (Preprint [1409.0544](#))
- [55] Bovard L and et al 2017 *in preparation*
- [56] Hanauske M, Takami K, Bovard L, Rezzolla L, Font J A, Galeazzi F and Stöcker H 2017 *Phys. Rev. D* (Preprint [1611.07152](#))
- [57] Alford M G, Bovard L, Hanauske M, Rezzolla L and Schwenzer K 2017 *arXiv:1707.09475* (Preprint [1707.09475](#))
- [58] Kastaun W, Ciolfi R and Giacomazzo B 2016 *Phys. Rev. D* **94** 044060 (Preprint [1607.02186](#))
- [59] Rezzolla L and Zanotti O 2013 *Relativistic Hydrodynamics* (Oxford, UK: Oxford University Press)
- [60] Nakamura T, Oohara K and Kojima Y 1987 *Progress of Theoretical Physics Supplement* **90** 1–218
- [61] Shibata M and Nakamura T 1995 *Phys. Rev. D* **52** 5428–5444
- [62] Baumgarte T W and Shapiro S L 1999 *Phys. Rev. D* **59** 024007 (Preprint [gr-qc/9810065](#))
- [63] Galeazzi F, Kastaun W, Rezzolla L and Font J A 2013 *Phys. Rev. D* **88** 064009 (Preprint [1306.4953](#))
- [64] Lattimer J M and Swesty F D 1991 *Nucl. Phys. A* **535** 331–376
- [65] Typel S, Röpke G, Klähn T, Blaschke D and Wolter H H 2010 *Phys. Rev. C* **81** 015803 (Preprint [0908.2344](#))
- [66] Brown D, Diener P, Sarbach O, Schnetter E and Tiglio M 2009 *Phys. Rev. D* **79** 044023 (Preprint [0809.3533](#))
- [67] Löffler F, Faber J, Bentivegna E, Bode T, Diener P, Haas R, Hinder I, Mundim B C, Ott C D, Schnetter E, Allen G, Campanelli M and Laguna P 2012 *Class. Quantum Grav.* **29** 115001 (Preprint [arXiv:1111.3344\[gr-qc\]](#))
- [68] Radice D, Rezzolla L and Galeazzi F 2014 *Mon. Not. R. Astron. Soc. L* **437** L46–L50 (Preprint [1306.6052](#))
- [69] Radice D, Rezzolla L and Galeazzi F 2014 *Class. Quantum Grav.* **31** 075012 (Preprint [1312.5004](#))
- [70]ourgoulhon E, Grandclément P, Taniguchi K, Marck J A and Bonazzola S 2001 *Phys. Rev. D* **63** 064029 (Preprint [gr-qc/0007028](#))
- [71] Radice D, Bernuzzi S and Ott C D 2016 *Phys. Rev. D* **94** 064011 (Preprint [1603.05726](#))
- [72] Foucart F, Deaton M B, Duez M D, O’Connor E, Ott C D, Haas R, Kidder L E, Pfeiffer H P, Scheel M A and Szilagyi B 2014 *Phys. Rev. D* **90** 024026 (Preprint [1405.1121](#))
- [73] Mewes V, Galeazzi F, Font J A, Montero P J and Stergioulas N 2016 *Mon. Not. R. Astron. Soc.* **461** 2480–2489 (Preprint [1605.02629](#))